Modeling and numerical simulations of lignite char gasification with CO2: The effect of gasification parameters on internal transport phenomena

Mehmet Karaca, Deniz Kaya, Ahmet Yozgatligil, Iskender Gökalp

Version of Record: https://www.sciencedirect.com/science/article/pii/S0016236120320639
Manuscript_0b9f4c5d437c641374dbde72e8e105d3

Modeling and numerical simulations of lignite char gasification with CO_2: the effect of gasification parameters on internal transport phenomena

Mehmet Karaca[a], Deniz Kaya[b,c] Ahmet Yozgatligil[b], Iskender Gökalp[b,c,*]

[a]Department of Aerospace Engineering, Middle East Technical University, 06800, Ankara, Turkey

[b]Department of Mechanical Engineering, Middle East Technical University, 06800, Ankara, Turkey

[c]Institut de Combustion Aérothermique Réactivité et Environnement, UPR3021, Centre National de la Recherche Scientifique, 45071, Orléans, France

*Corresponding author: iskender.gokalp@cnrs-orleans.fr

Abstract

The purpose of this study is to develop an experimental data-based char particle gasification model in order to assess the effects of particle size, gasification temperature and char generation heating rate on global gasification parameters. Also, the effect of initial porosity is observed by performing parametrical numerical simulations. A continuum-based model is used to solve the gasification inside a char particle and within the external boundary layer. The intrinsic rate of CO_2 gasification reaction is computed according to Langmuir-Hinshelwood (LH) mechanism. External mass transfer is modeled by Stefan-Maxwell relations, and Cylindrical Pore Interpolation Model (CPIM) is used for intra-particle molecular diffusion. In the model, all the effects due to particle internal structure changes are represented by a global conversion function, f(X) which is computed from local reaction rate values. In this study, f(X) is deduced from experimental results instead of phenomenological models almost impossible to validate. The best reproduction of the experimental gasification results is obtained for the function f(X) postulated as a summation of two Gaussian functions which represent the char particle random pore structures and their dynamics during gasification. Comparative simulation results show that the Gaussian for low conversion interval is shifted to even lower conversion values for higher gasification temperature and higher initial porosity. Thereby, the Gaussian function for low conversion rates (large particle sizes) is interpreted as representative of the diffusion-limited gasification regime in conjunction with the network of macropores and molecular diffusion rates. The modification of the pore structure due to char generation heating rates causes a shift of the second Gaussian towards higher conversion rates. It is therefore postulated that the second Gaussian function corresponds to the boundary layer diffusion-controlled regime related to available outer surface area of the particle.

Keywords: CO_2 gasification, modeling, lignite char, pore structure change.

Highlights:

- For modeling purposes, char internal structure changes can be expressed using an experimentally-determined function, f(X).
- Well reproduction of experimental results with the modeled f(X) function justifies the use of the sum of two Gaussians which separately represent the diffusion-limited and the boundary layer diffusion gasification regimes.
- The contribution of the pressure term in molecular transport, computed using Stefan-Maxwell equations, is found negligible.

1. Introduction

Coal is the largest source of global energy production, accounting for over 40 % of global power generation. A significant portion of the CO_2 emissions originates from the electricity generation and the commercial heat generation out of coal. Despite tightening limits on CO_2 emissions and the expansion of renewable technologies, coal production is still increasing [1,2]. Low-rank/high-ash coals are particularly responsible for particulate matter emissions. More efficient energy transition technologies with low carbon emissions are necessary. Coal gasification offers a cleaner and more effective conversion of low-rank/high-ash coals. Moreover, synthesis gas which is a product of gasification can directly be used for clean energy production processes. Low-rank coals are more reactive since they have a higher amount of mineral matter and a larger average pore size; which makes them a good candidate for gasification [3]. There is a substantial amount of both experimental and modeling work into the understanding of the reaction chemistry and the effect of structural evolution of coal particles on their gasification and combustion. In gasification studies, experimental work is conducted using equipment such as small size reactor beds, entrained flow type (drop tube) reactors, and thermogravimetric analyzers. Recent research has focused on the gasification and combustion under different temperatures and ambient gas composition [4]. Gasification (with CO_2) and the combustion (with O_2) rates at different conditions are observed with recent measurement methods [5]. The variation of gasification rate with the pore structure [6], and with the reactor pressure [7] were studied in entrained flow reactors. Simultaneous gasification with steam and CO_2 has drawn special attention recently [8,9]. In the context of steam/CO_2 gasification, influence of the coal char generation process [10,11], the influence of porosity [12], the volatile-char interactions [13], and the pressure [14,15] are investigated.

The gasification processes are categorized into three regimes by Smith [16] based on the governing physical and chemical mechanisms which determine the gasification rate. In a first regime, the chemistry solely controls gasification reactions which proceed uniformly on the particle inner surfaces. Larger particle sizes or higher reaction rates result in internal pore-diffusion limitations. In the second regime, the rate is controlled by the combined effects of pore diffusion resistance and surface gasification reactions. With further increase of the reaction rates the external boundary layer diffusion control of species concentration gradients sets in [16]. In this third regime, the gasification may be considered to occur at the outer surface of the particle. Here the external boundary layer, namely the Knudsen boundary layer, refer to the outer gas shell in which the molecular diffusion dominates the convective mass

transfer. The gasification regimes are determined by the particle properties such as particle size, particle porosity, pore structure, active site density etc., and the gasification atmosphere. The change in particle properties and the internal pore network are investigated experimentally in many studies for different gasification conditions [10,17–21]. Hungwe et al. studied high and low ash particles for CO_2 gasification and observed the change in porosity using Scanning Electron Microscopy (SEM) at different conversions [20]. They reported that surface area increases significantly up to 50 % conversion for both chars and for high ash particle (nearly 20 % ash), they observed the maximum area change between 50-75 % conversions. The surface area decreases in high ash particles because of pore coalescence and carbon accumulation within the pores in addition to the formation of macropores having lower surface areas due to the mesoporous structure. Nie et al. reported different pore shapes for various coal samples [17]. They concluded that different pore structures affect the adsorption and transport properties. For high volatile matter-containing coals (nearly 33 %), micropores increase while mesopores becomes significantly smaller. Jayaraman et al. reported that the char preparation heating rate affects the pore structure by changing the volatilization rate [10].

Experimental procedures only provide global measurements of the conversion, the change in composition in the gas phase, and observations of changing coal particle structure. On the other hand, numerical modeling can be used for the assessment of gasification and, similarly, the combustion processes within the coal particle and the boundary layer. Numerical models enable understanding the time variation of the internal porous structure and the gas composition inside the particle. Two commonly used approaches for simulation are the continuum and the discrete modeling.

The discrete modeling approach, which relies on the percolation theory, mainly accounts for the randomness of the pore structure and the heterogeneity of the particle composition. Discrete models are suited for the fragmentation analysis to predict the changes in the morphology during coal particle combustion and gasification. In the diffusion limited regime, percolation modeling may show the fragmentation behavior with a variation of the porosity [22] and the local Thiele modulus [23]. The transient increase in burning rate due to the morphology change can be analyzed using unsteady simulation [24]. The discrete models also enable the use of sub-models for the effect of ash mobility, ash diffusivity [25], the influence of swelling mechanism on gasification rates [26] and the ash agglomeration mechanism below ash fusion temperature [27].

The continuum models address the physics of the external flow with the boundary layer with or without taking into account the intraparticle mass transfer and gasification [28]. One-dimensional models without intraparticle mass transfer resolve the boundary layer with the surface and the gas-phase chemistry at steady [29] or transient conditions [30]. Recent work also provides highly resolved simulations of the flow around burning and gasifying coal particles [31,32].

The models, which consider the gas-solid reactions in the particle and the external boundary layer, solve spherically symmetric, one-dimensional reaction-diffusion equations. The one-dimensional reaction-diffusion model can be used for both the pore diffusion and the reaction limited regimes. The effect of pore structure evolution on the heterogeneous reaction rate is a main challenge in the continuum modeling approach. This problem can be solved by implementing simple models such as the random capillary model [33], the random pore model [34], or the adaptive random pore model [35], etc. Other sub-modeling approaches for the annealing, the peripheral fragmentation, and the ash agglomeration are alternatives to improve continuum models [35]. Additionally, a chemical looping mechanism could be assessed using a coupled one-dimensional quasi-steady model [36],[37].

With the continuum approach, Dai et al. used experimental conversion rate results to avoid submodels for the physical phenomena at a micro-scale [38]. This approach represents the local (spatially) dependence of the heterogeneous reactions on the variations of the particle inner structure by combining all non-modeled phenomena in a global function derived from experiments.

The present work focuses on CO_2 gasification of lignite char particles. The internal structure change function, f(X) is obtained from the experimental conversion vs. reaction rate data reported by Jayaraman and Gökalp [11] and then, it is modelled by the summation of two Gaussians. Starting from an initial guess for f(X) based on the experimental conversion data, optimization is performed by minimizing the differences between the experimental and modeled conversion vs time data. Following a similar approach as in [44], instantaneous quasi-steady gasification rate is calculated from Langmuir-Hinshelwood kinetics. The species conservation, the species diffusion and the momentum conservation equations are solved for both the inner porous field and the outer Knudsen boundary layer. The intraparticle mass transfer is modeled according to the Cylindrical Pore Interpolation Model (CPIM). The external mass transfer is modeled using Stefan-Maxwell relations. The effects on the particle internal structure changes of several parameters are investigated. They are the char generation

(pyrolysis) heating rate, the gasification temperature, the particle size, and the initial particle porosity.

2. Materials and methods

2.1. Experimental

The material used in this study is a high ash content Turkish lignite from the Thrace region in Turkey. The experimental data are taken from Jayaraman and Gökalp [11]. Ultimate and proximate analyses of the coal are given in Table 1 below.

Table 1. Proximate and ultimate analyses of Turkish lignite samples (based on dry basis wt. %) [11]

Proximate analysis	%
Ash	32.33
Volatile	36.40
Fixed carbon	21.70
Ultimate analysis	
C	54.34
H	3.74
N	1.57
S	3.74

In the reported work, the raw lignite particles were pre-dried and sieved to two mean diameters, 800 μm and 3 mm. The char particles were produced by pyrolysis in Ar atmosphere at the temperature used for gasification, i.e. 950 °C. During the pyrolysis procedure, the samples were heated with two heating rates, 100 K/min and 800 K/min, up to 950 °C and maintained for 5 minutes at this temperature. The recorded temperature and mass variations during the pyrolysis procedure are shown in Figure 1.

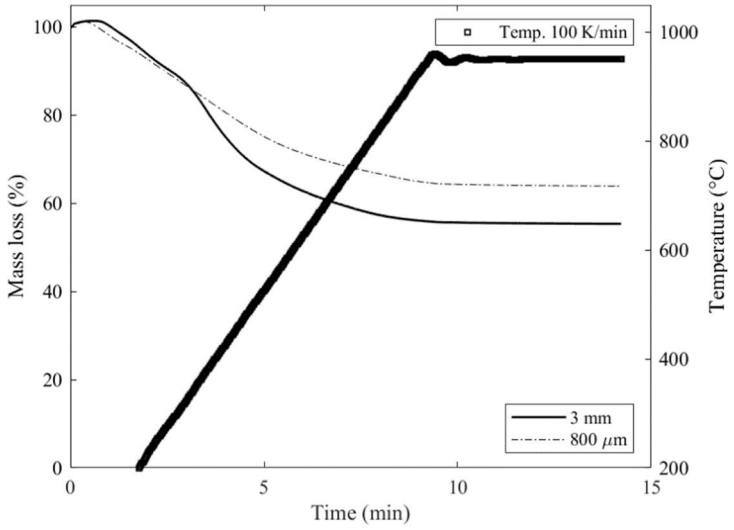

(a)

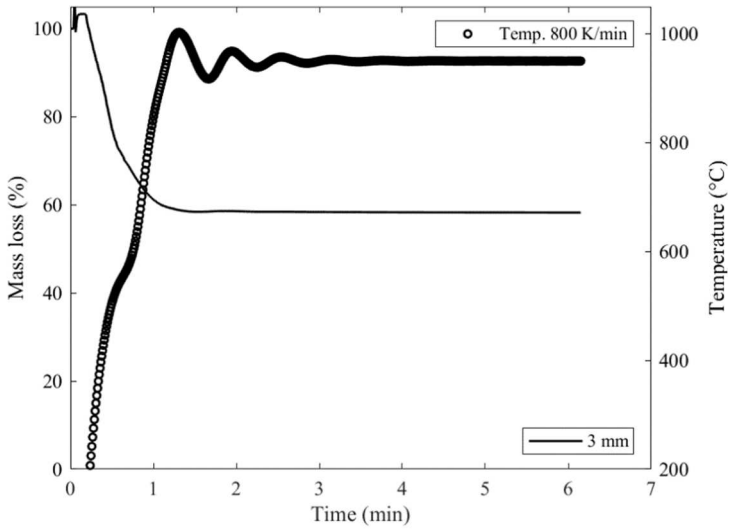

(b)

Figure 1. Mass loss during char generation and temperature variation under Ar atmosphere [11] (a) 3 mm and 800 μm particles at 100 K/min heating rate (b) 3 mm particle at 800 K/min heating rate

After pyrolysis, the char particles were cooled to room temperature. For their gasification experiments, they are first heated up to the target gasification temperatures with a lower heating rate of 40 K/min under Ar atmosphere. TGA gasification experiments in CO_2 were performed at 900 °C and 950 °C isothermally under 70 % CO_2 with balance Ar atmosphere for 800 μm and 3 mm particles (Figure 2a). Figures 2b and 2c show the change in the reaction rate and the conversion during gasification. The duration of gasification is shown to

be determined by the temperature. More detailed explanations of the experimental setup and procedure are reported in [39–41].

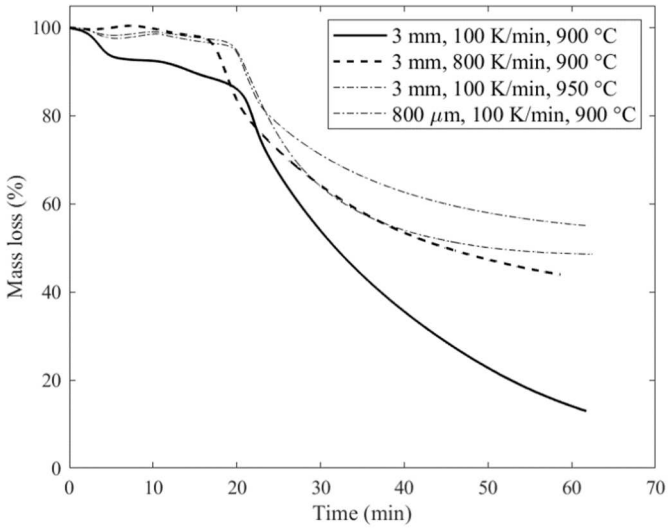

(a)

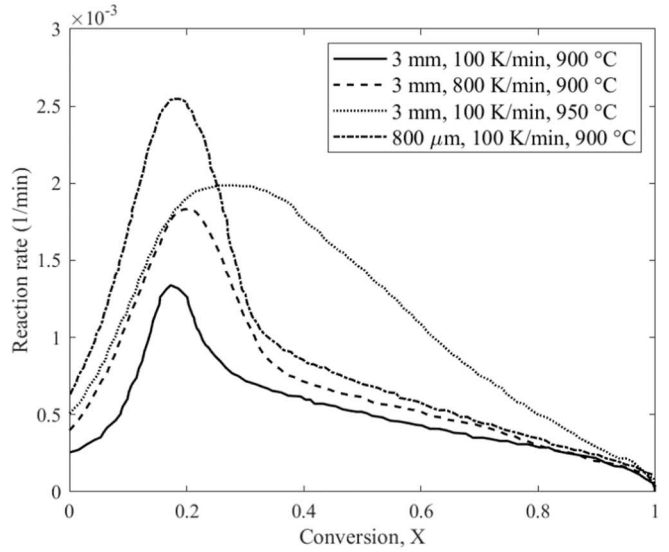

(b)

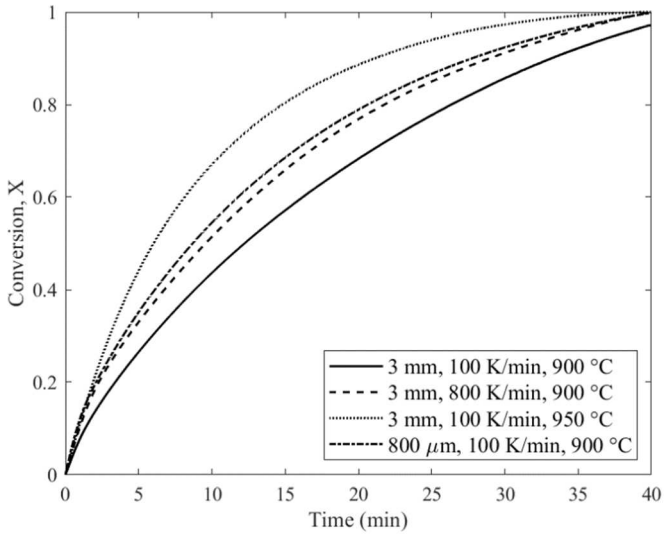

(c)

Figure 2. Experimental data for gasification in CO_2 [11] (a) Mass loss vs. time (b) Reaction rate variation with conversion (c) Conversion vs. time.

Experimental conditions considered in this study based on Jayaraman and Gökalp [11] are listed in Table 2.

Table 2. Overview of experimental parameters used in this study

	Particle size	Heating rate (K/min)	Gasification temperature (°C)	Gasification ambience
1	3 mm	100	900	70 % CO_2-Ar
2	3 mm	100	950	70 % CO_2-Ar
3	3 mm	800	900	70 % CO_2-Ar
4	800 µm	100	900	70 % CO_2-Ar

2.2. Numerical model

2.2.1. Modeling approach

The carbon conversion vs time is directly proportional to the rate of reaction, *r* and to the function f(X), which globally represents the change in the internal structure of the particle [42]:

$$\frac{dX}{dt} = r f(X) \quad (1)$$

The reaction rate, *r* can directly be expressed from the Arrhenius law considering only the overall Boudouard reaction $C_{(s)}+CO_{2(g)} \leftrightarrow 2CO_{(g)}$ for a char gasified by CO_2;

$$r = \mathrm{A}e^{-\frac{\mathrm{E_a}}{\mathrm{RT}}}\,\mathrm{g}(\mathrm{C_{react}}) \quad (2)$$

The overall reaction scheme is commonly used since the parameters, A and E_a, can easily be extracted from experimental data. However, char gasification with CO_2 is made of heterogeneous reactions occurring on pore surfaces via several steps of adsorption and desorption reactions. Moreover, due to the different morphological structures of the char particle, local heterogeneous reaction rates should also be calculated, including local parameters such as temperature, pressure, and concentration of species [43]. Therefore, it is more accurate to calculate the intrinsic rate of reaction according to the Langmuir-Hinshelwood (LH) mechanism [44–46]. For char gasification with CO_2, the commonly accepted two-step LH reaction scheme is reported by Ergun. In this scheme, first oxygen in CO_2 is adsorbed on the surface active-sites forming a surface oxygen complex (Eq. 3) and then, it evaporates together with the carbon atom as CO (Eq. 5) [46].

$$\mathrm{C^*_{(s)}} + \mathrm{CO_{2(g)}} \leftrightarrow \mathrm{C(O)} + \mathrm{CO_{(g)}} \quad (3)$$

$$\mathrm{C(O)} \rightarrow \mathrm{C^*_{(s)}} + \mathrm{CO_{(g)}} \quad (4)$$

The intrinsic reaction rate, *r,* of CO_2 char gasification according to LH mechanism can be calculated from [47]:

$$r = \frac{\mathrm{k_1 P_{CO_2}} + \mathrm{k_2 P_{CO_2}^2}}{1 + \mathrm{k_3 P_{CO_2}} + \mathrm{k_4 P_{CO}}} \quad (5)$$

where k_1, k_2, k_3, and k_4 are the temperature-dependent constants calculated by the Arrhenius law. Many studies reported experimentally-determined reaction parameters for the two-step LH mechanism for CO_2 gasification processes [42,44,47].

In Eq. 1, f(X) represents the changes in the internal structure of the char particle during gasification. There are many models reported in the literature for f(X). Commonly studied models are the volume reaction model, the shrinking core model (or sharp interface model), and the random pore model [48]. The choice of the model is crucial as the kinetic parameters will differ for each model. Moreover, porosity, voidage, active surface area and diffusivity parameters are not constant for the char particle during gasification. It is therefore essential to include the effects of the changes in such parameters in f(X) models. Due to the lack of detailed knowledge on the particle structural changes during different phases of gasification reactions, as also argued in [49], it is tempting to use the experimentally-determined f(X) function to globally model the local changes during the heterogeneous gasification reactions.

In the present work, the experimental reaction rate vs conversion data are used to compute an initial guess for the internal structure change function, f(X). This initial guess is composed of

the summation of two Gaussians. In this study, it is assumed that kinetically-controlled regime is passed and therefore, the first Gaussian is attributed to the gasification regime for which the gasification is controlled by both pore diffusion and kinetics. With the progress of gasification, char particle gets smaller and its porosity increases, so that the resistance due to pore diffusion diminishes. This is modeled with a second Gaussian to represent gasification regime in which the boundary layer diffusion is dominant. The initial pore structure as well as its various stages during gasification are assumed to be spatially random with an estimated average pore size. We postulate that this structure is best represented by a normal distribution. Six coefficients of the two Gaussians of f(X) are optimized by minimizing the differences between the experimental and modeled conversion vs. time data. This is performed iterating f(X) function by computing the reaction rate through solving the conservation equations. The governing equations for computations are reported in the following sections.

2.2.2. Governing equations

In this study, as in [44], char particle gasification is modeled with one-dimensional and spherically symmetric reaction-diffusion equations. Intraparticle temperature variations are neglected, and the Sherwood number is taken to be 2 for the mass transfer in the boundary layer. Three species are considered for the calculations: CO (α=1), CO_2 (α=2), and Ar (α=3).

Intraparticle conservation equations

· *Multispecies conservation equation:*

Within the char particle, the species mass balance is given by Eq. 6.

$$\frac{dJ_\alpha}{dr} = R_\alpha - \frac{2J_\alpha}{r} \quad (6)$$

$$R_\alpha = \frac{\nu_\alpha}{2} r_\alpha \rho_e f(X) \quad (7)$$

$$\rho_e = \rho_m(1-\varepsilon) \quad (8)$$

Here, J_α is the diffusion flux and R_α is the reaction rate for the species α. R_α is a function of the conversion. The bulk density of the particle, ρ_e can be calculated using porosity, ε, and the skeletal density of the particle, ρ_m. ν_α is the stoichiometric coefficient for the species α. The porosity change of a particle is calculated as a function of the conversion by;

$$\varepsilon(X) = \varepsilon_0 + X(1-\varepsilon_0) \quad (9)$$

In which ε_0 is the initial porosity of a particle and it is used here as a parameter with different values in order to see its effect on the fluxes. The multispecies equation is solved only for CO

since $J_{CO} + 2J_{CO_2} = 0$ and $J_{Ar} = 0$. In this study, the intrinsic reaction rate parameters are taken from Mühlen et al. [47].

· *Diffusion equation:*

Stefan-Maxwell equations are modified according to the Cylindrical Pore Interpolation Model (CPIM) and the mole fraction of species, x_α are calculated from the diffusion equation:

$$\frac{dx_\alpha}{dr} = \frac{\tau^2 RT}{\varepsilon P}\sum_{\beta=1}^{3}\left(\frac{x_\alpha J_\beta}{D_{A,\beta\alpha}} - \frac{x_\beta J_\alpha}{D_{A,\beta\alpha}}\right) - \frac{\tau^2}{\varepsilon P}x_\alpha\left(1 - \frac{1}{D_{Kn,\alpha}\sum_\beta \frac{x_\beta}{D_{Kn,\beta}}}\right)\nabla P \qquad (10)$$

Where R is the universal gas constant (8.314 J/mol.K) and τ is the tortuosity factor of the particle which is approached as $\sqrt{1/\varepsilon_0}$ [50]. T is the gasification temperature which is taken as constant according to experimental measurements. Pressure inside the particle, P, is simultaneously solved from the momentum equation (see below). $D_{A,\alpha\beta}$ is the effective diffusivity within pores calculated as an interpolation of the Knudsen diffusivity, $D_{Kn,\alpha}$ and the molecular diffusivity, $D_{B,\alpha\beta}$ [51].

$$\frac{1}{D_{A,\alpha\beta}} = \frac{1}{D_{Kn,\alpha}} + \frac{1}{D_{B,\alpha\beta}} \qquad (11)$$

The Knudsen diffusivity is taken from the kinetic theory, and the binary molecular diffusivities are computed using the Cantera software [52].

· *Momentum equation:*

The variation of pressure inside the particle is calculated from the momentum equation where the convection term is neglected

$$\frac{dP}{dr} = -\frac{\tau^2 A_A}{\varepsilon}\sum_{\beta=1}^{3}\left(\sqrt{M_\beta}.J_\beta\right) \qquad (12)$$

The pressure gradient coefficient, A_A, related to the molecular viscosity in porous media, is calculated from the relations given below for momentum transfer in Knudsen, A_{Kn} , and continuum, A_C , regimes [51]:

$$\frac{1}{A_A} = \frac{1}{A_{Kn}} + \frac{1}{A_C} \qquad (13)$$

$$A_{Kn} = \frac{3}{2d_{pore}}\sqrt{\frac{\pi RT}{2}} \qquad (14)$$

$$A_C = \frac{32\mu_{mix}RT}{Pd_{pore}^2\sum_{\alpha=1}^{3}(x_\alpha\sqrt{MW_\alpha})} \qquad (15)$$

d_{pore} is the pore diameter of a particle and in this study, is taken as constant and equal to 165 nm [38]. The dynamic viscosity of the gas mixtures is computed using Cantera software and updated along the radius [52]. MW_α indicates the molecular weights of CO, CO_2, and Ar.

· *Boundary conditions:*

As spherical symmetry is assumed, there is no flux for any species at the center of the particle;

$$J_{\alpha|r=0} = 0 \tag{16}$$

Since gas compositions at the edge of the external boundary layer are known, they are used to compute surface mole fractions;

$$x_{\alpha|r=r_p} = x_{\alpha,surf} \tag{17}$$

For the boundary layer, it is assumed that pressure is not changing and equal to the atmospheric pressure. Therefore, surface pressure is taken as 1 atm.

$$P_{|r=r_p} = P_{ambient} = 1\ atm \tag{18}$$

These surface conditions are used as boundary conditions for internal transfer equations.

External conservation equations

· *Multispecies conservation equation;*

In the boundary layer, the species conservation equation is:

$$\frac{dJ_\alpha}{dr} = -\frac{2J_\alpha}{r} \tag{19}$$

· *Diffusion equation:*

For the boundary layer, species mole fractions are calculated from the Stefan-Maxwell equations:

$$\frac{dx_\alpha}{dr} = \frac{RT}{P}\sum_{\beta=1}^{3}\left(\frac{x_\alpha J_\beta - x_\beta J_\alpha}{D_{B,\alpha\beta}}\right) \tag{20}$$

· *Momentum equation:*

It is assumed that pressure is constant in the boundary layer. Therefore, the momentum equation is simplified as:

$$\frac{dP}{dr} = 0 \tag{21}$$

· *Boundary conditions:*

The calculations are initiated with guessed $J_{\alpha,surf}$ values. After solving the internal transfer equations, the surface boundary condition for the CO flux is updated.

$$J_{\alpha|r=r_p} = J_{\alpha,surf} \tag{22}$$

The ambient compositions of gases and pressure are known; hence they are used as boundary conditions for external transfer equations;

$$x_{\alpha_{|r=r_p+\delta}} = x_{\alpha,\text{ambient}} \quad (\cong 0 \text{ for CO and} = 0.7 \text{ for } CO_2) \tag{23}$$

$$P_{|r=r_p+\delta} = P_{\text{ambient}} = 1 \text{ atm} \tag{24}$$

2.2.3. Numerical approach

In this study, MATLAB® is used to solve the set of equations (mass transfer, diffusion and momentum) for inside the particle and for the boundary layer. At X = 0, initial guess of coefficients for f(X) and of CO flux are optimized by minimizing the difference between the experimental and modeled conversion vs. time data using the MATLAB *lsqnonlin* function. This function is applicable to solve nonlinear least-square curve-fitting problems. For each set, governing equations are solved with a new f(X) using the MATLAB *bvp4c* function, which is a finite difference-based solver for boundary value problems. Governing equations for external transfer (mass balance for CO, external mass transfer for CO and CO_2, pressure) are first solved. Since the properties of gas flow in TGA experiments are fixed, boundary conditions at the edge of the boundary layer are used to find surface mole fractions and pressure conditions, taking the initial CO flux as the surface CO flux. Then, internal transfer equations (mass balance for CO, internal mass transfer for CO and CO_2, pressure) are solved with the surface boundary conditions, and the surface flux of CO is iterated. Finally, external transfer equations are solved again with the corrected surface CO flux. For following time steps and increasing conversion rates, the same solution procedure is followed using the MATLAB *fminsearch* function by optimizing the initial flux of CO to match the surface conditions from both external and internal parts.

3. Results and discussion

3.1. Gasification with CO_2

Radial variations of CO fluxes, CO mole fractions, and intraparticle pressure with respect to conversion rate are given in this section for the base case; 3 mm char particle size prepared at 100 K/min heating rate and gasified at 900 °C.

It should be noted that in all figures, dimensionless radius equals to 1 means the particle surface. The values below 1 correspond to the inner radial distance from the center of the particle while dimensionless radius values higher than 1 correspond to the outer radial distance in the boundary layer.

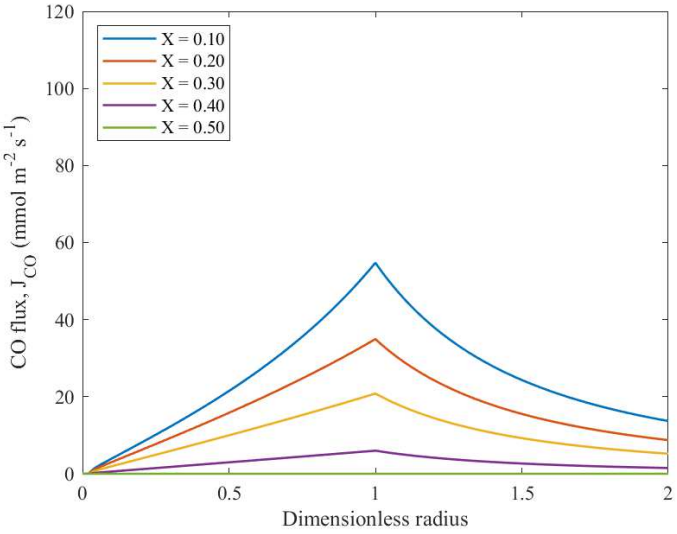
X = 0.10
X = 0.20
X = 0.30
X = 0.40
X = 0.50
CO flux, J_{CO} (mmol m^{-2} s^{-1})
Dimensionless radius

(a)

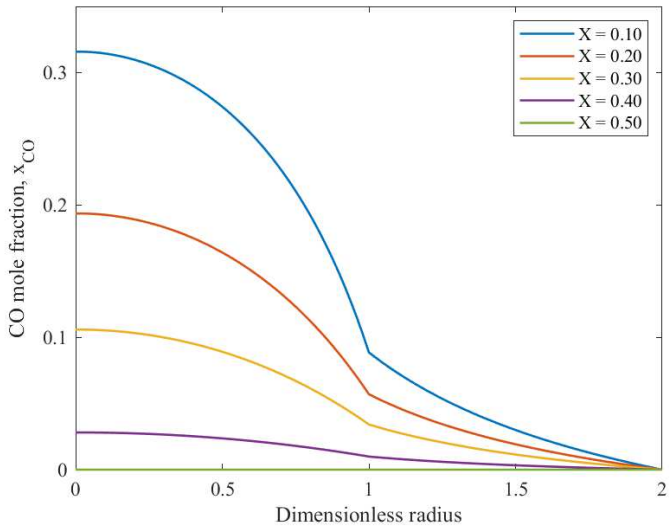
X = 0.10
X = 0.20
X = 0.30
X = 0.40
X = 0.50
CO mole fraction, x_{CO}
Dimensionless radius

(b)

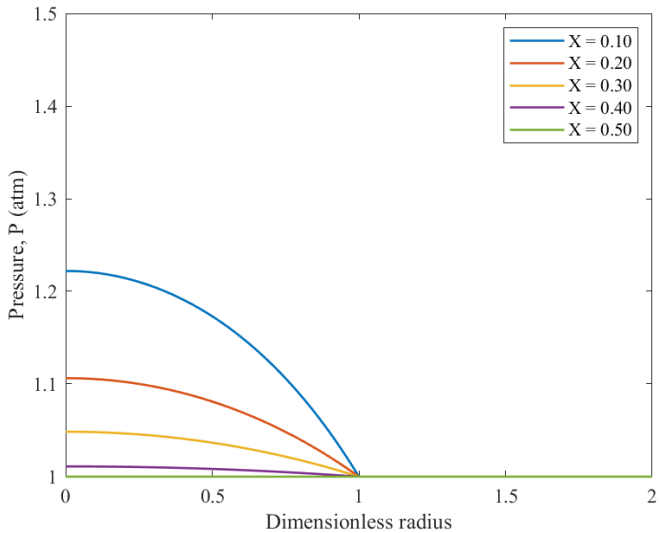
X = 0.10
X = 0.20
X = 0.30
X = 0.40
X = 0.50
Pressure, P (atm)
Dimensionless radius

(c)

Figure 3. (a) CO fluxes, (b) CO mole fractions and (c) intraparticle pressure at different conversion levels for 3 mm char particle with ε_0=0.33, prepared at 100 K/min heating rate under 70 % CO_2-Ar atmosphere and gasified at 900 °C

In Figure 3, it is observed that the CO fluxes are decreasing with increasing conversion. As reaction proceeds, the char particle is shrinking in size so that the gases cannot penetrate the solid particle which reduces the CO flux.

3.1.1. Effect of particle size

In order to observe the effect of particle size, the following two cases are compared; 3 mm and 800 μm particles gasified at 900 °C and prepared at 100 K/min heating rate.

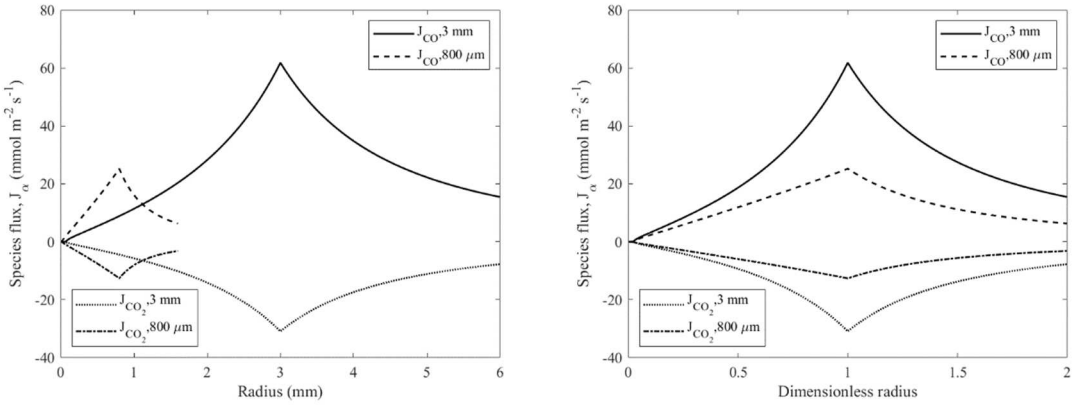

Figure 4. Comparison of the initial quasi-steady CO and CO_2 fluxes for 3 mm and 800 μm char particles with ε_0=0.33 generated with 100 K/min heating rate and gasified at 900 °C, under 70 % CO_2-Ar atmosphere

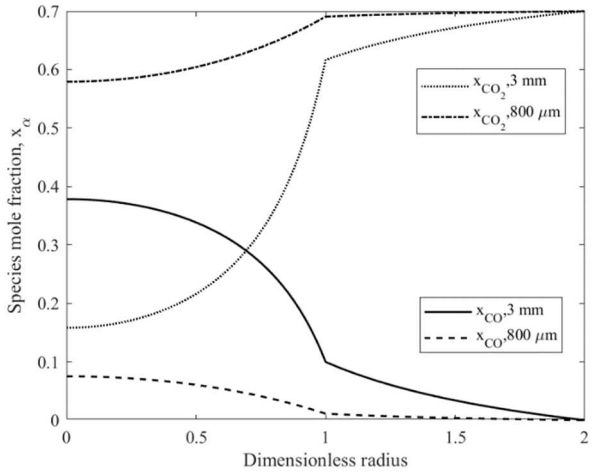

Figure 5. Comparison of the initial quasi-steady CO and CO_2 mole fractions for 3 mm and 800 µm char particles with ε_0=0.33 generated with 100 K/min heating rate and gasified at 900 °C, under 70 % CO_2-Ar atmosphere

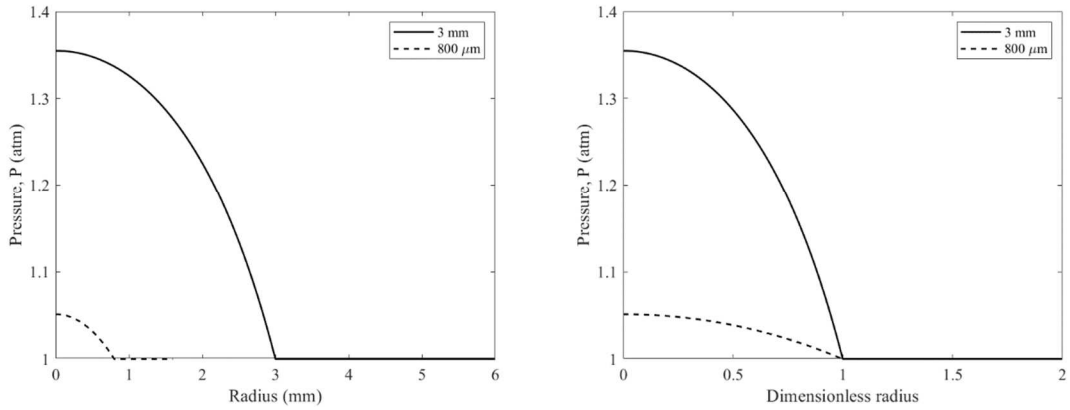

Figure 6. Comparison of the initial quasi-steady pressures for 3 mm and 800 µm char particles with ε_0=0.33 generated with 100 K/min heating rate and gasified at 900 °C, under 70 % CO_2-Ar atmosphere

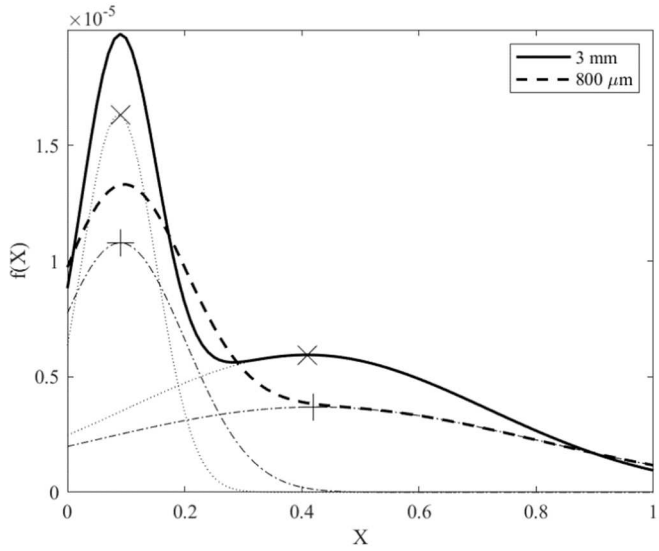

Figure 7. Comparison of f(X) for 3 mm and 800 µm char particles with ε_0=0.33 generated with 100 K/min heating rate and gasified at 900 °C, 70 % CO_2-Ar atmosphere (x and + markers indicate the Gaussian peaks for 3 mm and 800 µm, respectively.)

Smaller particles have a lower surface area but a higher surface to volume ratio. Consequently, active site density is expected to be higher for smaller particles except for the particles below a certain radius for which a relatively solid structure exists [53]. In Figure 4-6, the initial quasi-steady radial variation of the fluxes, the mole fractions and the pressure are shown for two different particle sizes. Figure 4 shows a higher rate of increase in CO flux for

smaller particles. However, as the stagnant Knudsen layer is shallow, ambient gas composition yields a lower CO surface composition along with a lower surface flux for smaller particles. Figure 6 shows a significant variation of internal pressure with particle size. The gasified matter accumulates within the particle due to the diffusion resistance of the porous wall which should result in a pressure increase within the particle. Nevertheless, the weight of the pressure gradient term in the momentum equation is observed to be negligible compared to the species gradient related diffusion term (Eq. 10).

The experimentally-determined function f(X), which indicates the global internal structure change, is fitted with two Gaussians. In Figure 7, the variation of f(X) by local conversion level is presented. The locations of maxima are not shifted for the two different size particles having the same experimental conditions. The particle specific surface is larger for small particles; thereby, the gasification is faster [54]. Also, due to the mesoporous structure, surface area increases because of the micropore formation especially at initial stages. For the particles prepared and treated under same conditions, it is expected that the trend of Gaussians should be the same while the area under the curve should change due to the availability of active surfaces for different size particles. It is observed from the Figure 7 that the effect of size is observed in the f(X) curve as larger areas under Gaussian functions having higher standard deviation for smaller particles. In other words, the peak point of Gaussians did not change significantly for different size of particles, while the area under the curve is observed to increase for a particle having larger diameter. A higher deviation yield flatter (smooth) change of gasification rate with the conversion. Nevertheless, the trend of the structural evolution is not affected much for both cases, as noted by Dai et al. [38]. This subtle difference in deviations is observed owing to the precision of TGA method.

3.1.2. Effect of heating rate

The effect of char generation heating rate is studied by comparing two different cases; for 3 mm particles prepared at100 K/min and 800 K/min heating rates and gasified at 900 °C.

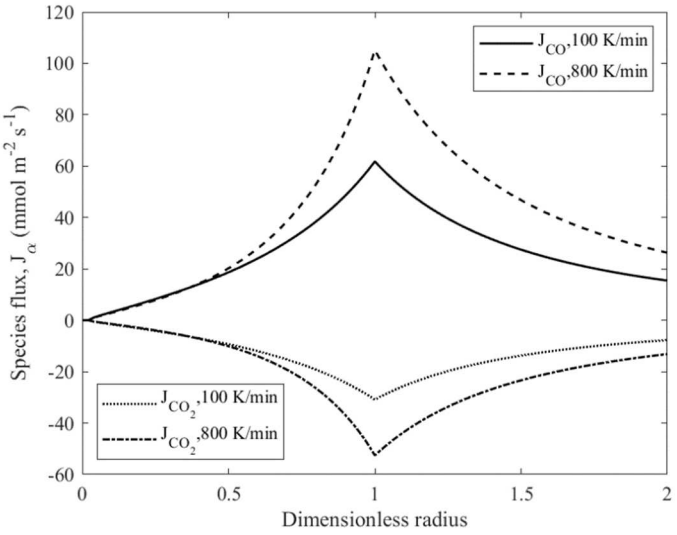

Figure 8. Comparison of the initial quasi-steady CO and CO_2 fluxes for 3 mm char particles with ε_0=0.33, generated with 100 K/min and 800 K/min heating rates and gasified at 900 °C, under 70 % CO_2-Ar atmosphere

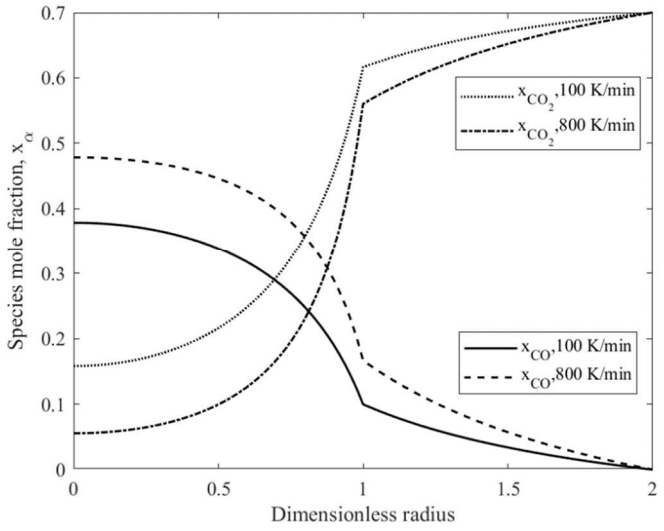

Figure 9. Comparison of the initial quasi-steady CO and CO_2 mole fractions for 3 mm particles with ε_0=0.33 generated with 100 K/min and 800 K/min heating rates and gasified at 900 °C, under 70 % CO_2-Ar atmosphere

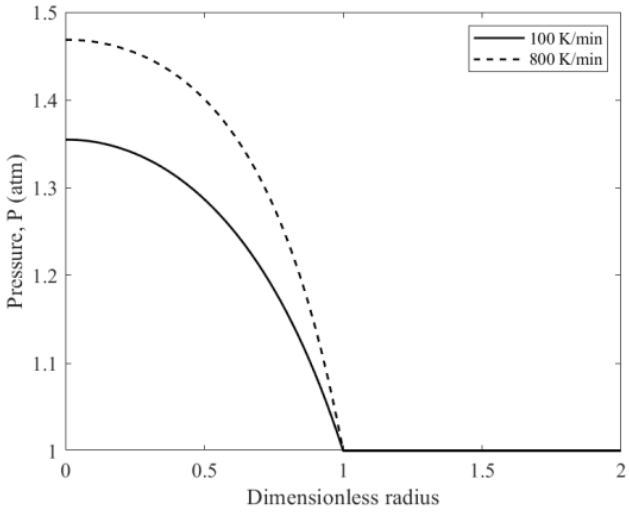

Figure 10. Comparison of the initial quasi-steady pressure for 3 mm char particles with ε_0=0.33 generated with 100 K/min and 800 K/min heating rates and gasified at 900 °C, under 70 % CO_2-Ar atmosphere

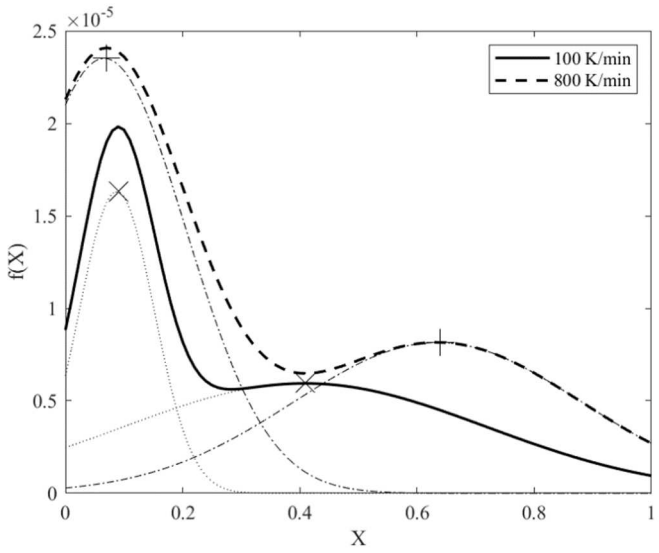

Figure 11. Comparison of f(X) for 3 mm char particles with ε_0=0.33 generated with 100 K/min and 800 K/min heating rates and gasified at 900 °C, under 70 % CO_2-Ar atmosphere (x and + markers indicate the Gaussian peaks for 100 K/min and 800 K/min, respectively.)

In real particle preparation processes, coal particles reach high temperatures almost instantly. However, heating rate analysis is essential to understand the physics of the gasification procedure. In Figure 8-10, the initial quasi-steady radial solution of the fluxes, the mole fractions, and the pressure are shown corresponding to gasification of particles prepared at different heating rates. Both the CO flux and the composition of CO are increasing within the

particle with radius, as reported in [55] that particles prepared at a higher heating rate gasify faster. It is observed that these particles yield higher intraparticle pressure, as seen in Figure 10. Figure 11 depicts the behavior of f(X) of particles prepared at different heating rates. The area under both curves increases with increasing heating rate, and the second peak is shifted to higher conversion rates for higher heating rates. The porous structure can be considered to consist of a network of cylindrical macropores and micropores in which cylindrical microrods are observed due to presence of highly dense network of solid microcrystals [56,57]. The two cases differ only for the preparation of particles in which the pore structure is modified. The structural alteration affects the second Gaussian function which may be attributed to boundary layer diffusion-limited regime of gasification. This can be explained by the fact that higher heating rates reduce the micropores and active surface sites giving a relatively smooth surface [58].

3.1.3. Effect of temperature

Two cases for different gasification temperatures are compared for a 3 mm char particle prepared at 100 K/min heating rate.

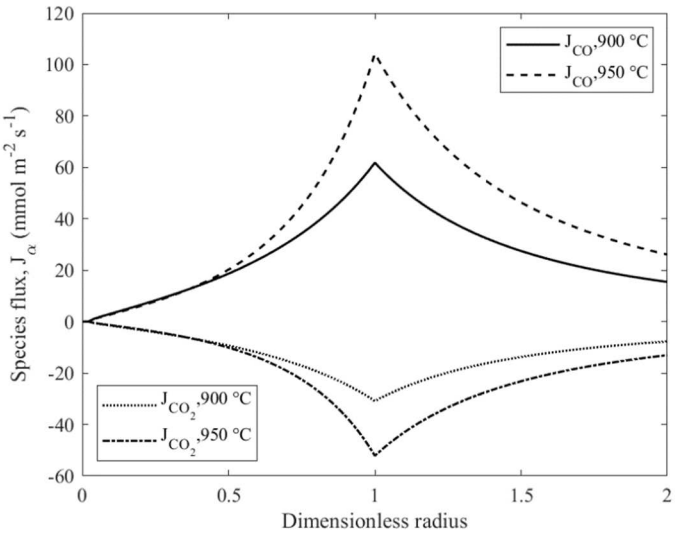

Figure 12. Comparison of the initial quasi-steady CO and CO_2 fluxes for 3 mm char particle with ε_0=0.33 generated with 100 K/min heating rate and gasified at 900 °C and 950 °C, under 70 % CO_2-Ar atmosphere

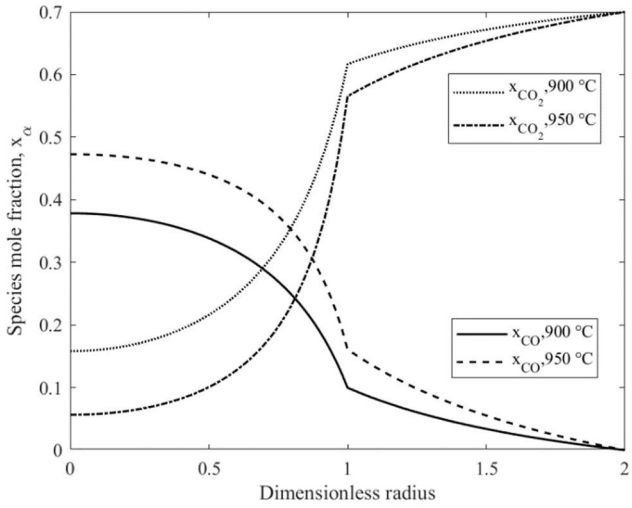

Figure 13. Comparison of the initial quasi-steady CO and CO_2 mole fractions for 3 mm char particle with ε_0=0.33 generated with 100 K/min heating rate and gasified at 900 °C and 950 °C, under 70 % CO_2-Ar atmosphere

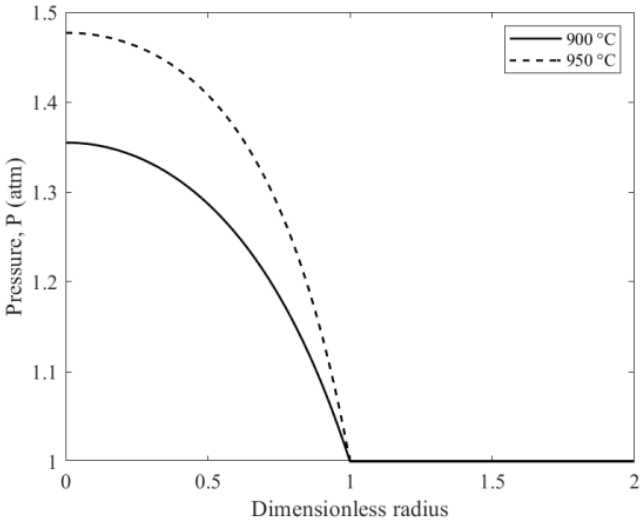

Figure 14. Comparison of the initial quasi-steady pressure for 3 mm char particles with ε_0=0.33 generated with 100 K/min heating rate and gasified at 900 °C and 950 °C, under 70 % CO_2-Ar atmosphere

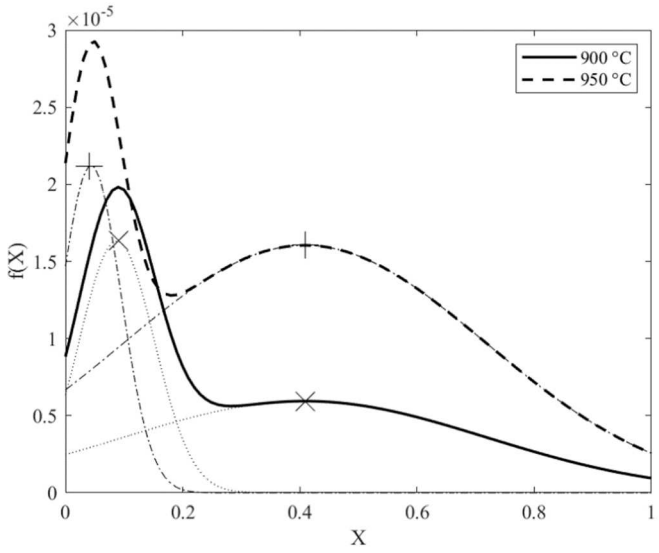

Figure 15. Comparison of f(X) for 3 mm char particle with ε_0=0.33 generated with a 100 K/min heating rate and gasified at 900 °C and 950 °C under 70 % CO_2-Ar atmosphere (x and + markers indicate the Gaussian peaks for 900 °C and 950 °C, respectively)

The gasification rate increases with the gasification temperature because of the temperature dependence of rate constants and molecular diffusivities. In Figure 12-14, the initial radial variation of the flux, the mole fractions, and the pressure are shown for two different gasification temperatures. Both the CO flux and the mole fraction of CO are higher for the 950°C gasification case. A higher gasification temperature case ends with a minor increase in internal pressure. It is seen from Figure 15 that the area under both curves increases with increasing temperature, and the first Gaussian is shifted to higher conversion rates for the higher temperature case, in contrast to Figure 11 where the char particle generation heating rate was changed for a constant char particle size. As the temperature dependence of the diffusion coefficients to temperature is (~7%) higher compared to reaction rate constant, the first Gaussian is observed to be shifted which is attributed to the diffusion of species in the pore network.

3.1.4. Effect of initial porosity

The effect of initial porosity of char particles on species transport is investigated for a 3 mm particle prepared at 100 K/min heating rate and gasified at 900 °C by varying parametrically the initial porosity as 0.25, 0.33, 0.50, and 0.67.

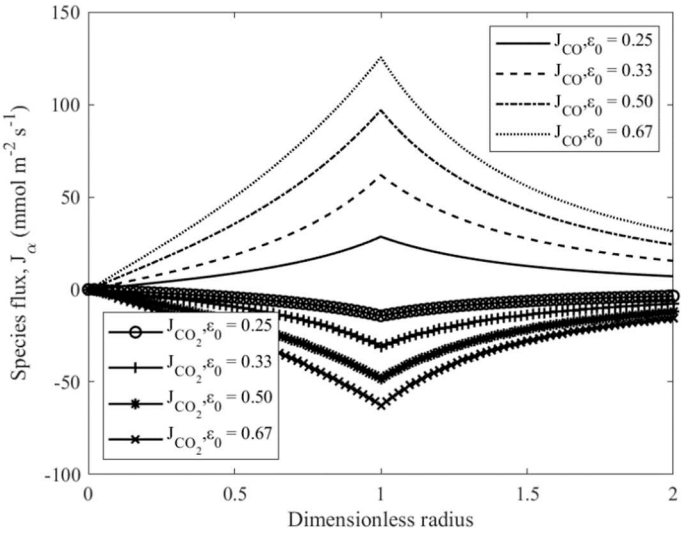

Figure 16. Comparison of the initial quasi-steady CO and CO_2 fluxes for various initial porosity values for a 3 mm char particle generated with 100 K/min heating rate and gasified at 900 °C, under 70 % CO_2-Ar atmosphere

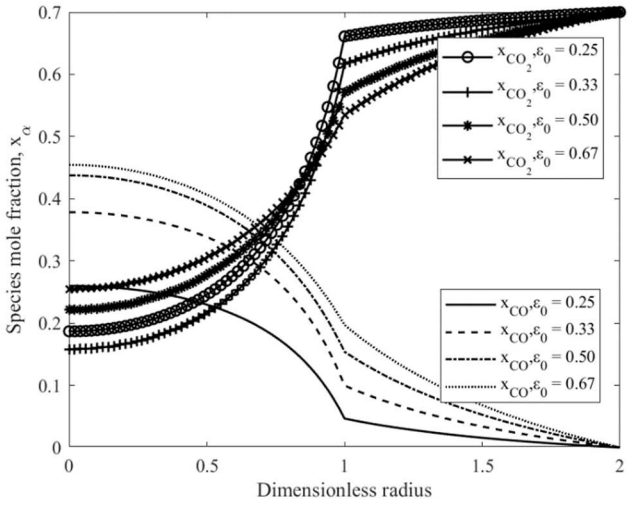

Figure 17. Comparison of the initial quasi-steady CO and CO_2 mole fractions for various initial porosity values for a 3 mm char particle generated with 100 K/min heating rate and gasified at 900 °C, under 70 % CO_2-Ar atmosphere

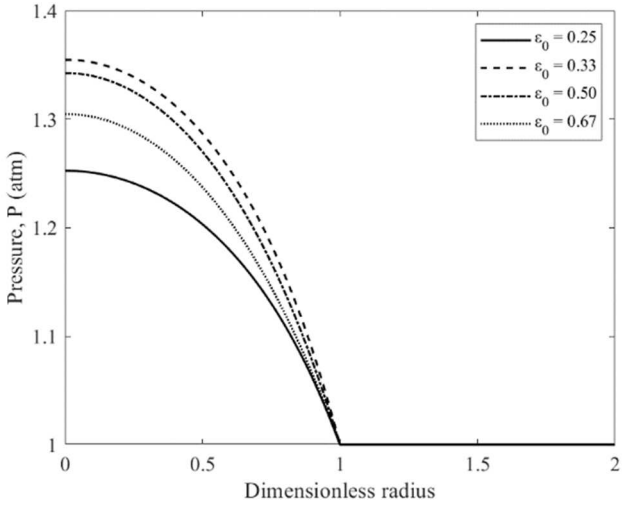

Figure 18. Comparison of the initial quasi-steady pressure for various initial porosity values for a 3 mm char particle generated with 100 K/min heating rate and gasified at 900 °C, under 70 % CO_2-Ar atmosphere

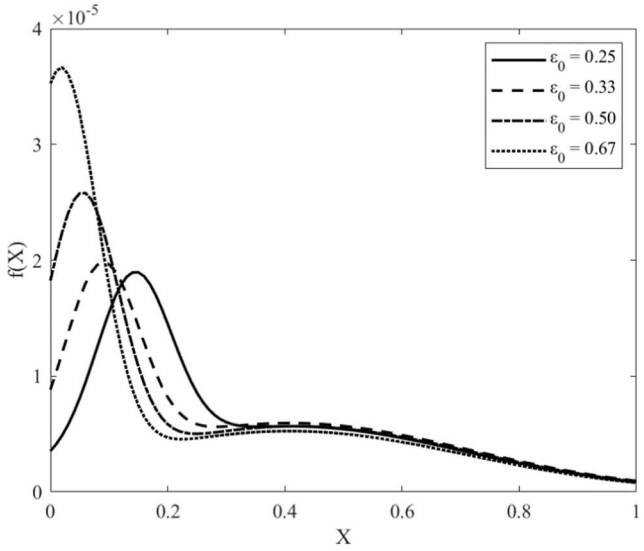

Figure 19. Comparison of f(X) for various initial porosity values for a 3 mm char particle generated with 100 K/min heating rate and gasified at 900 °C, under 70 % CO_2-Ar atmosphere

Figures 16-18 plot the species flux, mole fraction and the pressure in the radial axis for parametrically changes porosity values. Higher porosity provides more space for diffusion. The diffusion dominated early stages of conversion are augmented since the product CO is well evacuated. As the initial porosity takes larger values, it is observed from Figure 16 and Figure 17 that both the mass flux and the mole fraction of CO increase. Figure 19 shows that

as initial porosity increases, the first Gaussian is shifted to lower conversion values. This analysis confirms that the first Gaussian can directly be attributed to the initial pore opening due to the formation of micropores at the initial stages of gasification and increasing diffusion capacity of the porous structure.

3.1.5. Structure of function f(X)

In this study, function f(X) in Eq. 1 is interpreted from experimental conversion vs. time data, instead of using complicated and not really validated pore structure models. This function indicates the change in the particle internal structure globally and is computed from local composition and pressure values. The structure of this function is selected to represent the different stages of gasification and pore network change, as the summation of two Gaussians, given in Eq. 25 below.

$$f(X) = a_1 \exp\left[-\left(\frac{(X - b_1)}{c_1}\right)^2\right] + a_2 \exp\left[-\left(\frac{(X - b_2)}{c_2}\right)^2\right] \qquad (25)$$

Initial guess values for the parameters in f(X) are taken from the experimental conversion vs. reaction rate data [11]. However, it is known that these parameters are highly dependent on the reaction rate constants due to link between species fluxes, J_α and reaction rate, R_α Therefore, f(X) parameters are optimized in order to obtain logical results in terms of their order of magnitude. Consequently, the parameters in f(X) are optimized in each iteration while solving the system of equations so that the experimental conversion vs. time data are approached from the simulation results. Final optimized parameters for f(X) function are reported in Table 3 for each case.

Table 3. Parameters in f(X) function for each case

	Particle size	Heating rate (K/min)	Gasification temperature (°C)	f(X) parameters					
				$a_1 \times 10^5$	b_1	c_1	$a_2 \times 10^6$	b_2	c_2
1	3 mm	100	900	1.6344	0.0877	0.0902	5.9414	0.4087	0.4365
2	3 mm	100	950	2.1247	0.0438	0.0721	16.042	0.4087	0.1000
3	3 mm	800	900	2.3516	0.0663	0.1973	8.1499	0.6351	0.3469
4	800 µm	100	900	1.0793	0.0903	0.1569	3.6901	0.4239	0.5377

It should definitely be noted that reaction rate parameters have a significant effect on f(X) parameters. In this study, since the rate constants in LH reaction rate are taken from literature, only the trend of f(X) is discussed according to different experimental parameters.

4. Conclusions

A continuum-based model for char particle gasification was used to investigate the effect of char generation heating rate, gasification temperature, particle size and initial particle porosity. One dimensional spherically symmetric mass and momentum conservation equations for porous particle and external Knudsen layer were solved. The model was constructed on the idea of putting all unknown phenomena, which are related to the morphology change of solid particle, into a function of conversion, f(X). TGA experimental results of high-ash Turkish lignite were used to investigate the dependence of f(X) on the gasification parameters. Simulations were performed to determine f(X) that gives the best fit of experimental conversion data. Optimum f(X) functions were obtained as the sum of two separate Gaussian functions. The good agreement between the simulations and the experiments is achieved by optimizing the parameters of f(X) so that the changes inside particle structure are relevant to interpret the TGA data. Simulations provide radial variations of species diffusive fluxes, gas concentrations and intraparticle pressure. Therefore, the change of f(X) function can be correlated with the gasification conditions and the structural properties of the gasified material.

Higher gasification rates are observed; (i) when the char particles are generated with higher heating rates, (ii) for higher gasification temperatures, (iii) for smaller particle diameters and (iv) for higher particle porosities.

For smaller particles, CO mole fractions on the particle surface are smaller The Knudsen boundary layer is thinner; therefore, the CO concentration gradient is higher, resulting the evacuation of CO rapidly. The variation of f(X) with local conversion gives the same trend for particles of different sizes. However, varying the gasification temperature or the particle porosity affects the first Gaussian which is assumed to be related to pore diffusion-dominated regime. This is because molecular diffusion rates increase at higher temperatures. Also, researchers experimentally observed [17] that the mesoporous structure caused an increase in micropores during the initial stages of gasification, resulted in high surface areas offering more space for diffusion for high porosities. On the other hand, when comparing the results for the char particles generated at two different heating rates, one can observe that only the second Gaussian function is influenced. Therefore, the second Gaussian is attributed to

represent the boundary layer diffusion-limited gasification regime. This is due to the modifications of the structure of microrods and micropores. As the conversion increases, the pore diffusion becomes insignificant and the reaction takes place mainly at the surface of char particle. At this stage, only the diffusion of gases from far boundary layer to the particle surface becomes dominant.

As a last remark, it should be emphasized that the proposed structure of f(X) is a global representation of the char internal structure change during gasification without referring to the models given in the literature, i.e. shrinking core model, random pore model etc.. In this study, the species diffusion and reaction and the effects of them on the changes in the behavior of f(X) are investigated depending on several experimental parameters, so that the changes in pore network can be interpreted for gasification process. This current study can definitely be extended in order to propose an empirical model for f(X).

References

[1] IEA. Coal Information 2018. 2018. https://doi.org/10.1787/coal-2018-en.

[2] International Energy Agency. Energy Technology Perspectives 2017 - Executive Summary. 2017. https://doi.org/10.1787/energy_tech-2014-en.

[3] Radovic LR, Walker PL, Jenkins RG. Importance of catalyst dispersion in the gasification of lignite char. J Catal 1983;82:382–94.

[4] Gövert B, Pielsticker S, Kreitzberg T, Habermehl M, Hatzfeld O, Kneer R. Measurement of reaction rates for pulverized fuel combustion in air and oxyfuel atmosphere using a novel fluidized bed reactor setup. Fuel 2017;201:81–92. https://doi.org/10.1016/j.fuel.2017.03.009.

[5] Hu W, Marek E, Donat F, Dennis JS, Scott SA. A thermogravimetric method for the measurement of CO/CO2 ratio at the surface of carbon during combustion. Proc Combust Inst 2019;37:2987–93. https://doi.org/10.1016/j.proci.2018.05.040.

[6] Meng D, Wang T, Xu J, Chen X. Diffusion effect and evolution of kinetic parameters during coal char-CO2 gasification. Fuel 2019;255:115819. https://doi.org/10.1016/J.FUEL.2019.115819.

[7] Steibel M, Halama S, Geißler A, Spliethoff H. Gasification kinetics of a bituminous coal at elevated pressures: Entrained flow experiments and numerical simulations. Fuel 2017;196:210–6. https://doi.org/10.1016/j.fuel.2017.01.098.

[8] Jayaraman K, Gökalp I, Jeyakumar S. Estimation of synergetic effects of CO 2 in high ash coal-char steam gasification. Appl Therm Eng 2017;110:991–8. https://doi.org/10.1016/j.applthermaleng.2016.09.011.

[9] Li Y, Sun R, Wang M, Wang Z, Xu J, Ren X. Reaction kinetics of char-O2/H2O combustion under high-temperature entrained flow conditions. Fuel 2019;243:172–84. https://doi.org/10.1016/j.fuel.2019.01.109.

[10] Jayaraman K, Gokalp I, Bonifaci E, Merlo N. Kinetics of steam and CO 2 gasification of high ash coal-char produced under various heating rates. Fuel 2015;154:370–9. https://doi.org/10.1016/j.fuel.2015.02.091.

[11] Jayaraman K, Gokalp I. Effect of char generation method on steam, CO2 and blended mixture gasification of high ash Turkish coals. Fuel 2015;153:320–7. https://doi.org/10.1016/j.fuel.2015.01.065.

[12] Huo W, Zhou Z, Wang F, Wang Y, Yu G. Experimental study of pore diffusion effect on char gasification with CO2 and steam. Fuel 2014;131:59–65. https://doi.org/10.1016/j.fuel.2014.04.058.

[13] Kajitani S, Tay HL, Zhang S, Li CZ. Mechanisms and kinetic modelling of steam gasification of brown coal in the presence of volatile-char interactions. Fuel 2013;103:7–13. https://doi.org/10.1016/j.fuel.2011.09.059.

[14] Roberts DG, Harris DJ. Char gasification kinetics in mixtures of CO2 and H2O: The role of partial pressure in determining the extent of competitive inhibition. Energy Fuels 2014;28:7643–8. https://doi.org/10.1021/ef502101b.

[15] Zhang R, Wang QH, Luo ZY, Fang MX, Cen KF. Coal Char Gasification in the Mixture of H2O, CO2,H2, and CO under Pressured Conditions. Energy Fuels 2013;28:832–9. https://doi.org/10.3390/en12030496.

[16] Smith IW. Kinetics of combustion of size-graded pulverized fuels in the temperature range 1200–2270°K. Combust Flame 1971;17:303–14. https://doi.org/10.1016/S0010-2180(71)80052-4.

[17] Nie B, Liu X, Yang L, Meng J, Li X. Pore structure characterization of different rank coals using gas adsorption and scanning electron microscopy. Fuel 2015;158:908–17. https://doi.org/10.1016/j.fuel.2015.06.050.

[18] Gao M, Yang Z, Wang Y, Bai Y, Li F, Xie K. Impact of calcium on the synergistic effect for the reactivity of coal char gasification in H 2 O/CO 2 mixtures. Fuel 2017;189:312–21. https://doi.org/10.1016/j.fuel.2016.10.100.
[19] Fan C, Jin H, Shang F, Feng H, Sun J. Study on the surface structure development of porous char particles in catalytic supercritical water gasification process. Fuel Process Technol 2019;193:73–81. https://doi.org/10.1016/j.fuproc.2019.04.029.
[20] Hungwe D, Ding L, Khoshbouy R, Yoshikawa K, Takahashi F. Kinetics and Physicochemical Morphology Evolution of Low and High-Ash Pyrolytic Tire Char during CO_2 Gasification. Energy Fuels 2020;34:118–29. https://doi.org/10.1021/acs.energyfuels.9b03043.
[21] Yu G, Yu D, Liu F, Han J, Yu X, Wu J, et al. Different impacts of magnesium on the catalytic activity of exchangeable calcium in coal gasification with CO2 and steam. Fuel 2020;266:117050. https://doi.org/10.1016/j.fuel.2020.117050.
[22] Kerstein AR, Niksa S. Fragmentation during carbon conversion: Predictions and measurements. Symp Int Combust 1985;20:941–9. https://doi.org/10.1016/S0082-0784(85)80583-X.
[23] Salatino P, Miccio F, Massimilla L. Combustion and percolative fragmentation of carbons. Combust Flame 1993;95:342–50. https://doi.org/10.1016/0010-2180(93)90002-K.
[24] Kerstein AR, Edwards BF. Percolation model for simulation of char oxidation and fragmentation time-histories. Chem Eng Sci 1987;42:1629–34. https://doi.org/10.1016/0009-2509(87)80167-7.
[25] Miccio F, Salatino P, Tina W. Modeling Gasification and Percolation of Ash-Bearing Porous Carbon Particles. Proc Combust Inst 2000;28:2163–70. https://doi.org/10.1111/0022-1082.00184.
[26] Suzuki K. The contest for leadership in East Asia: Japanese and Chinese approaches to outer space. Space Policy 2013;29:99–106. https://doi.org/10.1016/j.spacepol.2013.03.006.
[27] Lin S, Ding L, Zhou Z, Yu G. Discrete model for simulation of char particle gasification with structure evolution. Fuel 2016;186:656–64. https://doi.org/10.1016/j.fuel.2016.09.011.
[28] Haugen NEL, Mitchell RE, Tilghman MB. A comprehensive model for char particle conversion in environments containing O2 and CO2. Combust Flame 2015;162:1455–63. https://doi.org/10.1016/j.combustflame.2014.11.015.
[29] Mitchell RE, Kee RJ, Glarborg P, Coltrin ME. The effect of CO conversion in the boundary layers surrounding pulverized-coal char particles. Symp Int Combust 1991;23:1169–76. https://doi.org/10.1016/S0082-0784(06)80377-2.
[30] Lee JC, Yetter RA, Dryer FL. Transient numerical modeling of carbon particle ignition and oxidation. Combust Flame 1995;101:387–98. https://doi.org/10.1016/0010-2180(94)00207-9.
[31] Farazi S, Sadr M, Kang S, Schiemann M, Vorobiev N, Scherer V, et al. Resolved simulations of single char particle combustion in a laminar flow field. Fuel 2017;201:15–28. https://doi.org/10.1016/j.fuel.2016.11.011.
[32] Kriebitzsch S, Richter A. LES simulation of char particle gasification at Reynolds numbers up to 1000. Combust Flame 2020;211:185–94. https://doi.org/10.1016/j.combustflame.2019.08.028.
[33] Gavals GR. A random capillary model with application to char gasification at chemically controlled rates. AIChE J 1980;26:577–85. https://doi.org/10.1002/aic.690260408.

[34] S.K B, Perlmutter DD. A Rondom Pore Model for Fluid-Solid Reactions : 1 . Isothermal , Kinetic Control. AIChE J 1980;26:379–86.
[35] Singer SL, Ghoniem AF. Comprehensive gasification modeling of char particles with multi-modal pore structures. Combust Flame 2013;160:120–37. https://doi.org/10.1016/j.combustflame.2012.09.007.
[36] Saucedo MA, Lim JY, Dennis JS, Scott SA. CO2-gasification of a lignite coal in the presence of an iron-based oxygen carrier for chemical-looping combustion. Fuel 2014;127:186–201. https://doi.org/10.1016/j.fuel.2013.07.045.
[37] Saucedo MA, Butel M, Scott SA, Collings N, Dennis JS. Significance of gasification during oxy-fuel combustion of a lignite char in a fluidised bed using a fast UEGO sensor. Fuel 2015;144:423–38. https://doi.org/10.1016/j.fuel.2014.10.029.
[38] Dai P, Dennis JS, Scott SA. Using an experimentally-determined model of the evolution of pore structure for the gasification of chars by CO 2 Orthogonal Collocation on Finite Element. FUEL 2016;171:29–43. https://doi.org/10.1016/j.fuel.2015.12.041.
[39] Jayaraman K, Gökalp I. Thermal characterization, gasification and kinetic studies of different sized Indian coal and char particles. Int J Adv Eng Sci Appl Math 2014;6:31–40. https://doi.org/10.1007/s12572-014-0104-z.
[40] Kandasamy J, Gŏkalp I. Pyrolysis, combustion, and steam gasification of various types of scrap tires for energy recovery. Energy Fuels 2015;29:346–54. https://doi.org/10.1021/ef502283s.
[41] Jayaraman K, Gökalp I. Pyrolysis, combustion and gasification characteristics of miscanthus and sewage sludge. Energy Convers Manag 2015;89:83–91. https://doi.org/10.1016/j.enconman.2014.09.058.
[42] Everson RC, Neomagus HWJP, Kasaini H, Njapha D. Reaction kinetics of pulverized coal-chars derived from inertinite-rich coal discards: Gasification with carbon dioxide and steam. Fuel 2006;85:1076–82. https://doi.org/10.1016/j.fuel.2005.10.016.
[43] Laurendeau NM. Heterogeneous kinetic of coal char gasification and combustion. Prog Energy Combust Sci 1978;4:221–70. https://doi.org/10.1016/0360-1285(78)90008-4.
[44] Gadsby J, Long FJ, Sleightholm P, Sykes KW. The mechanism of the carbon dioxide-carbon reaction. Proc R Soc Lond Ser Math Phys Sci 1948;193:357–76. https://doi.org/10.1098/rspa.1948.0051.
[45] Ergun S. Kinetics of the reaction of carbon with carbon dioxide. J Phys Chem 1956;60:480–5. https://doi.org/10.1080/00405846509541970.
[46] Strange JF, Walker PL. Carbon-carbon dioxide reaction: Langmuir-Hinshelwood kinetics at intermediate pressures. Carbon 1976;14:345–50. https://doi.org/10.1016/0008-6223(76)90008-7.
[47] Mühlen HJ, van Heek KH, Jüntgen H. Kinetic studies of steam gasification of char in the presence of H2, CO2 and CO. Fuel 1985;64:944–9. https://doi.org/10.1016/0016-2361(85)90149-8.
[48] Molina A, Mondragón F. Reactivity of coal gasification with steam and CO 2. Fuel 1998;77:1831–9. https://doi.org/10.1016/S0016-2361(98)00123-9.
[49] Dai P, Dennis JS, Scott SA. Using an experimentally-determined model of the evolution of pore structure for the gasification of chars by CO2. Fuel 2016;171:29–43. https://doi.org/10.1016/j.fuel.2015.12.041.
[50] Petersen EE. Diffusion in a pore of varying cross section. AIChE J 1958;4:343–5. https://doi.org/10.1002/aic.690040322.
[51] Young JB, Todd B. Modelling of multi-component gas flows in capillaries and porous solids. Int J Heat Mass Transf 2005;48:5338–53. https://doi.org/10.1016/j.ijheatmasstransfer.2005.07.034.

[52] Goodwin D. CANTERA: An Object-oriented Software Toolkit for Chemical Kinetics, Thermodynamics, and Transport Processes, Caltech, Pasadena 2009.
[53] Kibria MA, Sripada P, Bhattacharya S. Rational design of thermogravimetric experiments to determine intrinsic char gasification kinetics. Proc Combust Inst 2019;37:3023–31. https://doi.org/10.1016/j.proci.2018.07.085.
[54] Jayaraman K, Gokalp I. Effect of char generation method on steam, CO2 and blended mixture gasification of high ash Turkish coals. Fuel 2015;153:320–7. https://doi.org/10.1016/j.fuel.2015.01.065.
[55] Jayaraman K, Gokalp I. Effect of char generation method on steam, CO 2 and blended mixture gasification of high ash Turkish coals. Fuel 2015;153:320–7. https://doi.org/10.1016/j.fuel.2015.01.065.
[56] Kantorovich II, Bar-Ziv E. Processes in highly porous chars under kinetically controlled conditions: II. Pore reactivity. Combust Flame 1994;97:79–87. https://doi.org/10.1016/0010-2180(94)90117-1.
[57] Kantorovich II, Bar-Ziv E. Processes in highly porous chars under kinetically controlled conditions: I. Evolution of the porous structure. Combust Flame 1994;97:61–78. https://doi.org/10.1016/0010-2180(94)90116-3.
[58] Bai Y, Lv P, Yang X, Gao M, Zhu S, Yan L, et al. Gasification of coal char in H 2 O/CO 2 atmospheres: Evolution of surface morphology and pore structure. Fuel 2018;218:236–46. https://doi.org/10.1016/j.fuel.2017.11.105.